Robust analysis of space-, time-, and energy-resolved soft x-ray measurements of magnetically confined fusion plasmas (invited)

P. D. VanMeter,[1, a)] L. F. Delgado-Aparicio,[2] L. M. Reusch,[1, b)] and D. J. Den Hartog[1]
[1)]*Department of Physics, University of Wisconsin-Madison, Madison, WI, 53706, USA*
[2)]*Princeton Plasma Physics Laboratory (PPPL), Princeton, NJ, 08540, USA*

A novel compact multi-energy soft x-ray (ME-SXR) diagnostic based on the PILATUS3 100K x-ray detector has been developed in collaboration between the Princeton Plasma Physics Laboratory and the University of Wisconsin-Madison, and tested on the Madison Symmetric Torus (MST) reversed-field pinch. This solid-state photon-counting detector consists of a two-dimensional array of ∼100,000 pixels for which the lower photon absorption cutoff energy can be independently set, allowing it to be configured for a unique combination of simultaneous spatial, spectral, and temporal resolution of approximately 1 cm, 100 eV, and 500 Hz, respectively. The diagnostic is highly versatile and can be readily adapted to diverse plasma operating conditions and scientific needs without any required downtime. New results from improved-confinement and quasi-single helicity plasmas in the MST demonstrate how the detector can be applied to study multiple aspects of the evolution of magnetically confined fusion-grade plasmas. These include observing the evolution of thermal emissivity, characterizing the energy of mid-Z excitation lines, extracting the T_e profile, and observing the evolution of non-thermal populations. A technique for integrating the ME-SXR into an integrated data analysis framework based on Bayesian inference is also presented. This allows ME-SXR measurements to be combined with data for complimentary diagnostics in order to simultaneously infer T_e and n_Z using all available information.

I. INTRODUCTION

The Multi-Energy Soft X-ray (ME-SXR) project aims to develop a single versatile x-ray diagnostic suitable for multiple applications in the study of magnetically-confined fusion plasmas. Developed in cooperation with the Princeton Plasma Physics Lab, the diagnostic is based on a compact pinhole camera using a custom calibration which allows the lower threshold for photon detection to be adjusted on a per-pixel level. This allows for a novel synthesis of spatial resolution, spectral resolution, and versatility by carefully adjusting the pixel thresholds *in-situ* to configure the detector to best suit a given physics task (SEC. II). Multiple applications of the detector are presented in this paper, including studying profile evolution (SEC. III), diagnosing impurities (SEC. IV), characterizing T_e (SEC. V), and analyzing non-thermal populations (SEC. VI). A method for integrating ME-SXR other diagnostics using a Bayesian framework is also presented (SEC. VII).

Following a proof-of-concept implementation at Alcator C-Mod[1], the ME-SXR diagnostic was developed and tested on the Madison Symmetric Torus (MST)[2]. The MST is a medium-sized reversed-field pinch located on the campus of the University of Wisconsin-Madison. It features a unique conductive aluminum shell which permits self-organizing behavior. This also results in the presence of significant population of aluminum ions in the plasma bulk, affecting the soft x-ray spectrum. The defining characteristic of the reversed-field pinch (RFP) is that the magnetic field is mostly toroidal in the core, like the tokamak, but twists around as you move out in radius before reversing near the edge. This results in the presence of unstable $m = 1$ tearing modes in the core, which increases plasma stochasticity and transport. However, by making use of an improved confinement scenario called Pulsed Poloidal Current Drive[3,4] (PPCD), the MST can produce fusion-relevant plasmas, achieving temperatures as high as 2 keV and densities of approximately 10^{19} m^{-3}. A significant population of soft x-rays (SXR) are emitted in this regime, resulting primarily from bremsstrahlung and radiant recombination between the electron and ion populations. The presence of partially-ionized aluminum ions from the shell also contribute strong emission lines to the spectrum at around 2 keV. These properties make the MST into an interesting testbed for a new soft x-ray diagnostic. Additionally, a robust set of existing diagnostics allow for complementary measurements and useful comparisons.

Three additional papers relevant to the ME-SXR project are contained in these proceedings: L.F. Delgado-Aparicio, *et al.* further considers the analysis of data on the MST[5]; O. Chellai, *et al.* describes the calibration of a ME-SXR detector for the WEST tokamak[6]; and T. Barbui *et al.* describes the calibration of a multi-energy hard x-ray (ME-HXR) detector for WEST[7].

II. THE ME-SXR DIAGNOSTIC

The ME-SXR diagnostic is based on the PILATUS3 100K-M, a pixelated hybrid photon-counting x-ray detector produced commercially by DECTRIS Ltd. and specifically modified for PPPL. The device is composed of a single 450 μm Si sensor which absorbs incident photons, producing a cloud of photoelectrons with a total charge proportional to the photon energy[8]. This charge is then transferred via a bump-bonded indium connection to one of the many charge-sensitive preamplifiers (CSA) located on one of the 16 application-specific integrated circuits (ASIC) that compose the detector. The charge is converted to a pulse which is discriminated against a threshold by a comparator, rejecting photons with energies below the threshold. The threshold is controlled by a global comparator V_{cmp} setting, but can be further adjusted, or trimmed, on an individual level by an additional setting stored in a 6-bit register called the "trimbit" setting. Pulses which pass this threshold are recorded into a 20-bit counter and read out at pre-set intervals. These ASICs are arranged in an 8x2 grid, each contain an array of 60x97 individual pixels (each with its own CSA, comparator, trimbit setting, and counter), leading to a total of 480x194 = 93,120 pixels (often referred to as 100k). Individual pixels have an effective area

[a)]Currently at Department of Radiology, Mayo Clinic, Rochester, MN, USA; Electronic mail: VanMeter.Patrick@mayo.edu
[b)]Also at Edgewood College, Madison, WI, USA

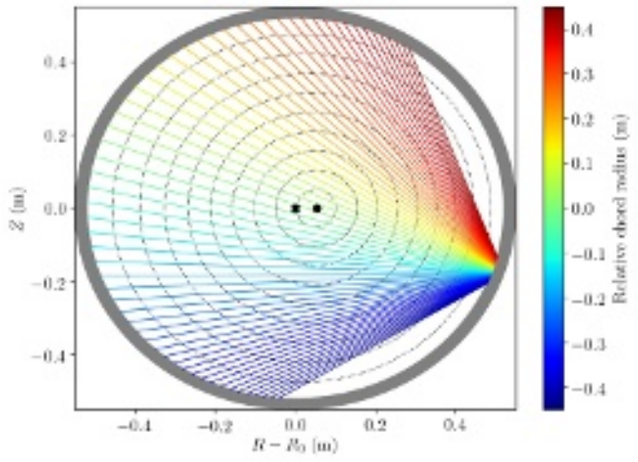

FIG. 1. Impact parameter for ME-SXR lines of sight within a poloidal plane, as determined by the spatial calibration. Due to space considerations only $1/8^{th}$ of the total 487 vertical chords are shown. Positive impact parameter increases as the line of sight moves upward in the MST vessel. The "X" designates the geometric axis of the MST, and the circular point designates the magnetic axis assuming a 6 cm Shafranov shift. Typical flux surfaces are also shown.

of 172×172 μm^2. The detector is installed with radial view of the the through a rectangular pinhole-like opening.

The silicon thickness sets an upper limit of about 30 keV, and the lower limit is set by placing an 25 μm Be filter over the pinhole. An additional 100 μm Mylar filter was also installed to reduce the overall photon flux and prevent saturation[9]. The integration time can be set to as low as 1 ms, and the electronics readout takes an additional 1 ms, resulting in an effective time resolution of up to 500 Hz. Spatial resolution is limited by the pinhole geometry to about 1 cm in the core. An *in-situ* spatial calibration was performed by exposing the detector to an Fe-55 source attached to a retractable probe. The resulting chord geometry is illustrated in FIG. 1.

Energy thresholds were calibrated via a custom procedure by exposing the detector to a series of fluorescence targets with strong lines at pre-selected energies and scanning the trimbit settings[10]. This data was used to create a mapping between energy threshold (E_c) and trimbit setting for each pixel. Multiple custom multi-energy configurations were developed, including high SNR 1D imaging, high radial resolution 1D imaging, and 2D "metapixel" imaging[11].

III. TIME EVOLUTION OF PLASMA SOFT X-RAY EMISSION

In normal operation, the ME-SXR records a series of images at the selected cycle rate, usually 500 Hz. Once an image is recorded, the data can be separated into one-dimensional SXR emission profiles in the poloidal plane according to threshold. The evolution of these profiles over time can provide significant insight into the heating and profile evolution of a plasma.

An example of data taken with eight simultaneous thresholds is shown in FIG. 2, which depicts the evolution of a single PPCD (improved confinement) plasma. Three full profiles are shown, with lower thresholds of 4, 5, and 6 keV, and the evolution of the core-most chord is shown for all eight thresholds. Initially the SXR emissivity is very low, corresponding to a low T_e. However once the PPCD period begins, driving $J_\parallel$ and thereby suppressing core tearing mode activity and reducing thermal transport, the plasma emissivity begins to increase rapidly. This emissive structure gradually broadens as the plasma bulk continues to heat. This comes to a sudden end at approximately 21 ms, once the PPCD banks have discharged all of their available energy. The "improved confinement" period rapidly collapses as the return of tearing modes allows the stored thermal energy to rapidly transport out of the core, cooling the plasma and thereby terminating the emissivity structure.

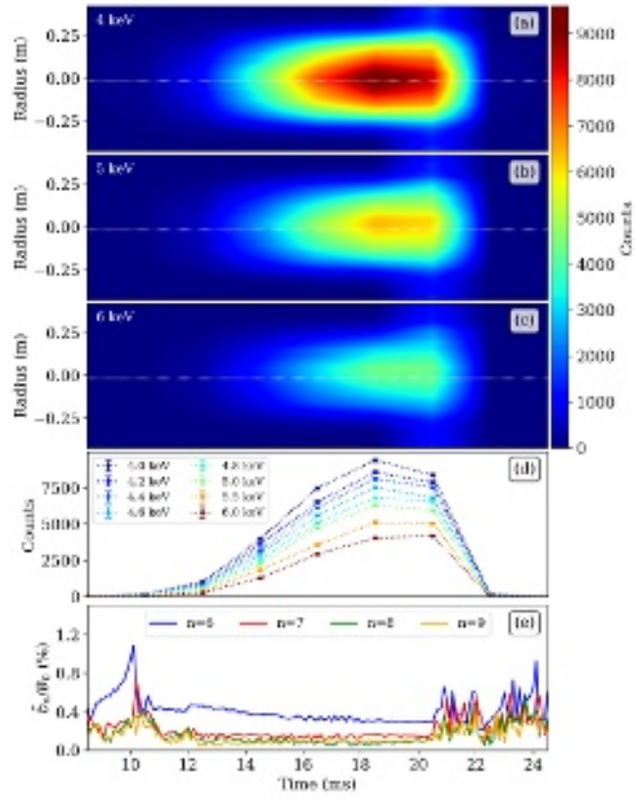

FIG. 2. Evolution of observed soft x-ray emission during a single PPCD discharge. Panels (a), (b), and (c) depict the profile evolution for $E_c = 4,5,6$ keV respectively. Panel (d) depicts the evolution of the core-most chords for all eight profiles, corresponding to the white dashed lines in the previous panels. Panel (e) depicts the evolution of the $m = 1$ magnetic spectrum, identifying the increased emission with the suppression of tearing mode activity.

IV. DETECTION OF MID-Z IMPURITIES

The ME-SXR diagnostic can also be used to identify the presence of mid-Z impurities in the plasma. Such impurities will be partially ionized and typically feature strong emission lines comfortably within the SXR range, which can be discerned by a proper selection of thresholds. This was tested by injecting small amounts of argon gas into non-reversed plasmas as a pre-fill, allowing the gas to diffuse throughout the vacuum vessel before the plasma is formed. For typical MST parameters, Ar features strong emission lines around 3 keV[12]. The ME-SXR diagnostic allows us to set thresholds both

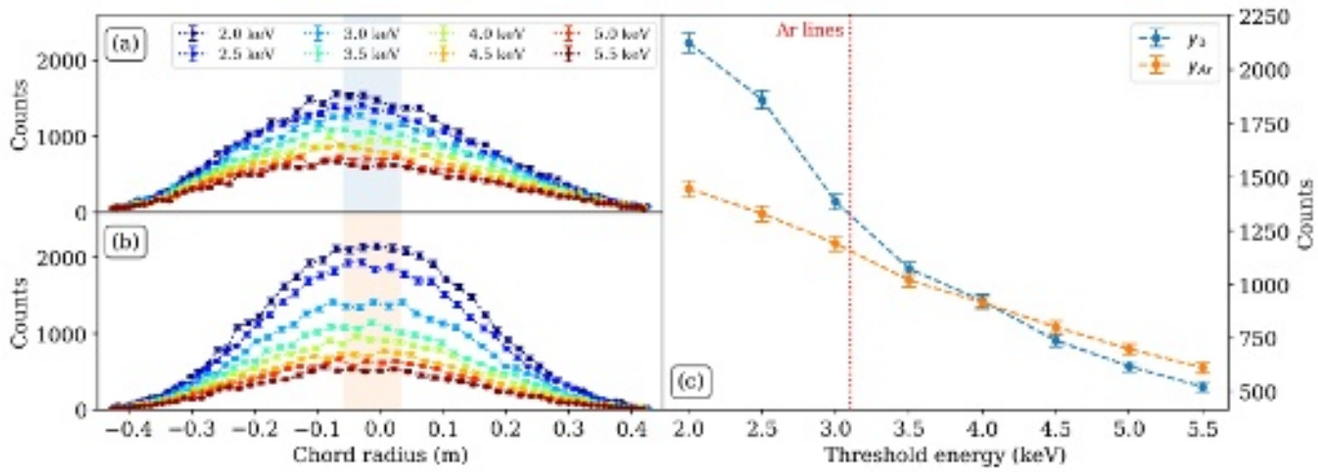

FIG. 3. Frames from two non-reversed plasmas (a) without and (b) with an injected argon dopant, with otherwise similar plasma characteristics. Increased emission is for thresholds below the 3 keV Ar emission lines. (c) Measured single frame spectrum (counts vs lower threshold) for similar non-reversed plasmas with and without an argon pre-fill. Counts are averaged over central chords (highlighted regions in (a) and (b)). The dominant emission line energy for argon is denoted by a vertical red line.

above and below this energy allowing for a direct detection of these photons.

FIG. 3 shows single-frame eight-color 1D measurements for two similar plasmas, except that (b) features the argon dopant and (a) is argon-free. The counts for $E_c \leq 3$ keV increase substantially when argon is present, while for higher energies the measurements are comparable. This comparison is shown more clearly in FIG. 3 (c), which shows the photon counts (averaged over five central chords) vs the threshold energy for each case. This clearly demonstrates that the increased signal is entirely due to Ar emission lines, meaning that the concentration of argon is low enough to not substantially change Z_{eff} (which would affect all thresholds). This demonstrates that the ME-SXR diagnostic can be used as an *ad-hoc* spectrometer to diagnose the presence of mid-Z like Ar impurities in the plasma.

The difference in the measured spectra can be used to positively identify argon as the source of the increased emissivity. Since the two spectra are very similar for $E_c > 3$ keV, we will assume that the entire difference in signal is due to the presence of an additional source of photons of a single characteristic energy, E_0. We will denote the two spectra shown in FIG. 3 (c) as $\boldsymbol{y}_{Ar}$ and $\boldsymbol{y}_0$ for the Ar-doped and clean measurements, respectively. Then, the difference, $\boldsymbol{d} = \boldsymbol{y}_{Ar} - \boldsymbol{y}_0$, approximately forms an S-curve, just like those encountered during the energy calibration procedure[10]. This is shown as the data points in FIG. 4. Points for $E_c > 4$ keV were set to zero since Ar lines will not contribute significant signal for these thresholds.

The S-curve traced out by $\boldsymbol{d}$ can be fit directly to an S-curve model like that used in the energy calibration. The chosen model includes a simple linear model of charge-sharing[9] and an S-curve width of $\sigma_E = 0.3$ keV, both determined by the calibration. That leaves a model with two free parameters, the amplitude N_{50} and the source energy E_0, given by

$$N(E_c; N_{50}, E_0) = \frac{N_{50}}{2}\left[\text{erf}\left(-\frac{E_c - E_0}{\sigma_E\sqrt{2}}\right) + 1\right] \times \Big(1 + k\cdot\big(E_c - E_0\big)\Big). \tag{1}$$

The charge-sharing slope k is related to the line energy $k = -2f/E_0$, where $f = 0.266$ is the ratio of the pixel area where charge sharing occurs to the total pixel area (see L.F. Delgado-Aparicio, *et al.*'s contribution to these proceedings for a more thorough description of this treatment[5]).

In order to properly account for counting statistics, the model parameters were determined using Bayesian inference[13] (discussed in more detail in Section VII) with a Poisson likelihood function,

$$\ln \mathscr{L}(\boldsymbol{\theta}) = -\sum_{i=1}^{N}\left[N_i - d_i \ln N_i + \ln(d_i!)\right]. \tag{2}$$

where d_i is the data point for the i$^{\text{th}}$ chord and the parameters $N_i = N(E_{c,i}|N_{50}, E_0)$ are equated to Equation 1 for the appropriate threshold. We will assume independent uniform priors, $N_{50} \sim \mathscr{U}(300, 700)$ and $E_0[keV] \sim \mathscr{U}(2, 5.5)$, denoted by $\boldsymbol{\pi}(N_{50})$ and $\boldsymbol{\pi}(E_0)$. Then, the posterior distribution is given by Bayes' Rule as $p(N_{50}, E_0|\boldsymbol{d}) \propto \mathscr{L}(N_{50}, E_0)\,\boldsymbol{\pi}(N_{50})\,\boldsymbol{\pi}(E_0)$. Since we are only interested in the source energy, we will marginalize N_{50} out as a nuisance parameter to obtain

$$p(E_0|\boldsymbol{d}) = \int p(N_{50}, E_0|\boldsymbol{d})\, dN_{50}. \tag{3}$$

This distribution is shown by the red curve in FIG. 4.

The resulting posterior distribution is very narrowly peaked, with a 1σ credible interval of $E_0 = 3.05 \pm 0.02$ keV, though this estimate does not account for variability between plasma discharges. This E_0 is very close to the energy of the brightest line of Ar^{+16}. Since

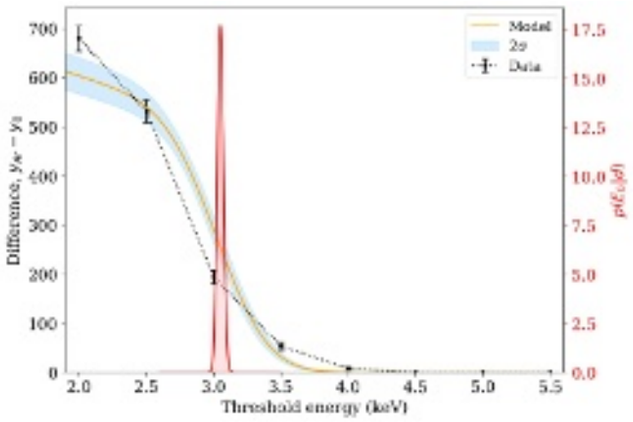

FIG. 4. The difference between the two spectra shown in FIG. 3 (c) form an S-curve which can be used to determine the source energy E_0 to within 40 eV. The black points are the measured data $\boldsymbol{d}$, the best-fit model is shown with a 95% confidence region, and the posterior distribution over E_0 is shown in red. The narrowness of this distribution shows a high confidence in the results.

the He-like state is often the most common ionization state of mid-Z impurities in the plasma core, this measurement would be sufficient to identify the impurity (or at least narrow the range of candidates). FIG. 4 also shows the fit between the model (Equation 1) and the measured data $\boldsymbol{d}$, with error bars representing the 95% confidence level. Agreement is not perfect, but some discrepancy is expected given that the reference signal $\boldsymbol{y}_0$ was taken from a different plasma discharge than $\boldsymbol{y}_{Ar}$. In situations where the variability between plasma discharges can be further reduced, accuracy can presumably be improved. The PILATUS3 can be calibrated for thresholds up to $E_c > 20$ keV, making this technique applicable to a wide range of impurities.

V. TEMPERATURE PROFILE ANALYSIS

There are multiple techniques that could be employed to infer the electron temperature profile from ME-SXR data. In situations where circular symmetry can be assumed a straightforward Abel inversion can be used to extract the emissivity profile[14] for each threshold, which are then related to T_e directly via ratios. The method presented here is similar to this approach, but employs a Bayesian methodology to systematically propagate uncertainty and account for non-cylindrical flux surface geometries. It relies upon prior knowledge of the profile shape, which can be a drawback in some situations.

In general, the count rate detected by a cluster of pixels indexed by i on the ME-SXR with a shared threshold E_c and plasma volume is related to the local photon emissivity rate via line integral

$$N_{\gamma,i}(p,\phi) = \eta_i \int_{\mathscr{L}(p,\phi)} \varepsilon_\gamma(z)dz, \tag{4}$$

where p and ϕ are the tangency radius and angle which parameterize the chord, η_i is the pixel étendue[15], and z parameterizes the distance along the chord.

This equation can be recast as a matrix equation which maps the emissivity as a function of flux radius $\varepsilon_\gamma(\rho)$ to the measured photon count rates for each cluster of pixels $N_{\gamma,i}$ using a flux surface reconstruction code (such as MSTfit[16]).

The next step is to choose a model for the emissivity profile. We will select a 3-parameter $\alpha-\beta$ profile which is commonly used for the RFP[17]. This profile shape assumes a relatively flat core which then decreases monotonically around the mid-radius before going to zero at the edge.:

$$\varepsilon(\rho) = \varepsilon_0(1-\rho^\alpha)^\beta. \tag{5}$$

This shape has the advantage that it forces the core of the profile to be flat, stabilizing the ratio. However parameterizations of other forms could be used instead, or possibly even nonparametric models based on Gaussian processes[18].

Next, the task is to constrain the profile parameters given the measured data by sampling the posterior distribution. Sampling also allows for a direct computation of profile uncertainty. This procedure was performed for a single frame recorded during of 300 kA PPCD operations, and the resulting emissivity profiles for a single 300 kA PPCD plasma are shown in FIG. 5 (a). The profile is flat in the core out to $r/a \approx 0.4$ before decreasing to near-zero at around $r/a \approx 0.8$.

These emissivity profiles, and their associated uncertainties, can be used to produce estimates of the electron temperature by considering the ratio of the observed emissivity at a given point in the radial profile relative to a chosen reference threshold. If we assume that the threshold energy is sufficiently high to justify ignoring emission lines and recombination steps then the emissivity (up to a multiplicative constant) is given by the energy integral $\mathscr{I}$,

$$\begin{aligned}\mathscr{I}(T_e,E_c) &\equiv \int_0^\infty \frac{e^{-E/T_e}}{E\sqrt{T_e}} R(E;E_c)dE \\ &\propto \varepsilon_\gamma(T_e;E_c),\end{aligned} \tag{6}$$

where $R(E;E_c)$ is the total pixel response function which accounts for transmission through filters, absorption into Si, and energy discrimination due to detector electronics as a function of the chosen threshold (or "cutoff energy") E_c. When taking the ratio of two emissivity profiles the multiplicative constants cancel out, leaving a ratio of the energy integrals,

$$\begin{aligned}\mathscr{R}(T_e,E_c) &= \frac{\varepsilon_\gamma(T_e,E_c)}{\varepsilon_\gamma(T_e,E_{ref})} \\ &= \frac{\mathscr{I}(T_e,E_c)}{\mathscr{I}(T_e,E_{ref})},\end{aligned} \tag{7}$$

where E_{ref} is threshold corresponding to the reference profile selected to serve as the denominator.

Using these ratio curves the electron temperature may be directly inferred. The measured ratio for each threshold > 3 keV was used to infer T_e, and these individual inferences were averaged (weighted by uncertainty) to produce an overall estimation of T_e and its uncertainty. This process was repeated at each radial point to produce a profile. The resulting profile is shown in FIG. 5 (b) along with corresponding Thomson scattering points for reference. Comparison in

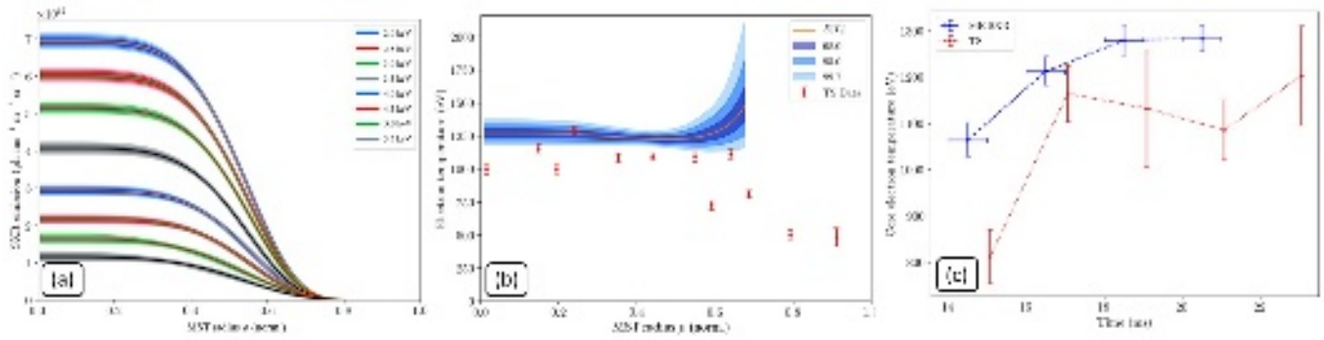

FIG. 5. (a) Reconstructed emissivity profile as a function of ρ, the MSTfit radius-like normalized flux surface label. (b) Reconstructed electron temperature profile as a function of ρ compared to simultaneous Thomson scattering data. Profiles are similar from the core to mid-radius, though the ME-SXR technique tends to produce poor results nearer the edge. (c) Evolution of the average core temperature over time for this plasma discharge compared to Thomson.

the core to mid-radius is generally favorable, but $r/a = 0.6$ the profile begins to increase unphysically. However soft x-ray emission from this far out in the radial profile tends to be very low due to the declining electron density, so this portion of the profile is mostly constrained by low count rates and is therefore subject to significant noise. As a result, values for T_e for $\rho > 0.6$ are be omitted. FIG. 5 (c) extends this analysis to multiple time points during the improved confinement period, showing that, as expected, the core temperature is consistently increasing.

This methodology was used to individually analyze an ensemble of 35 individual 300 kA PPCD shots, each including three time points. The core T_e for each point was then compared against the corresponding Thomson scattering measurement. As suggested by the individual profile inversion shown in FIG. 5, the temperature inferred from ME-SXR data is systematically higher than the Thomson measurements by $\Delta T_e \approx 180$ eV on average. The source of the 180 eV offset has not been determined, though the effect of high-energy photons originating from a non-Maxwellian electron population (known to be present in PPCD[19]) is a possible candidate. Regardless of the source, because the offset is constant (and therefore independent of the incident photon rate) it is not a result of detector saturation. Therefore, we can treat ΔT_e as a calibration factor. Using this methodology, ME-SXR measurements can be used to effectively determine the evolution of T_e over time.

VI. RUNAWAY ELECTRONS

Although the most of this paper focuses on the diagnosis of plasma thermal properties, the ME-SXR diagnostic can also be used to characterize non-thermal properties. The 450 μm Si sensor is sensitive to photons up to around 30 keV, allowing higher-energy x-rays emitted by runaway electrons to be detected. This section presents observations from one such study on the MST.

Under the conditions of high current and low density, RFP plasmas may spontaneously transition into a helical equilibrium. This state is characterized by a magnetic spectrum largely (thought not entirely) dominated by a single toroidal tearing mode, and is therefore called "Quasi-Single Helicity" (QSH)[20]. Previous studies on the RFX-mod RFP have shown that QSH is associated with improved thermal confinement and the formation of transport barriers[21]. The

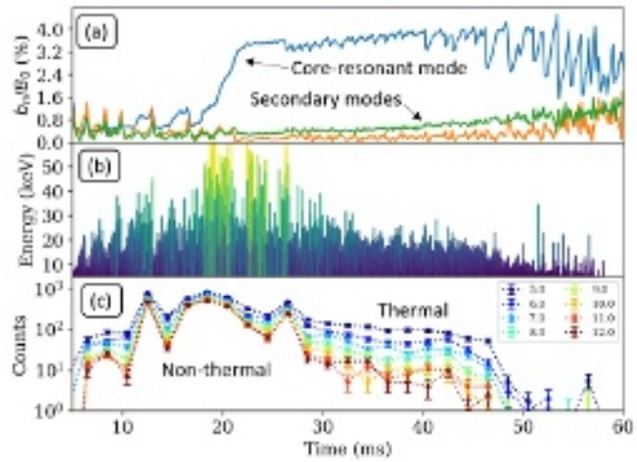

FIG. 6. (a) Magnetic signals during a QSH plasma in the MST. (b) Measurements made with a dedicated single-chord fast x-ray detector, represented by pulses whose heights are proportional to photon energy. (c) simultaneous measurements from the ME-SXR core-most chords

presence of runaway electrons in QSH plasmas in the MST was briefly studied in a 2010 paper by Clayton *et al.*[22].

These observations were extended by the ME-SXR diagnostic. The detector was configured into an eight-color high SNR configuration using the the medium gain calibration[10] which allows for thresholds between 4-to-14 keV. The thresholds were set to $E_c = 5$, 6, 7, 8, 9, 10, 11, and 12 keV. This configuration allows for some sensitivity to thermal electrons on the low end, but also extends into the hard x-ray range. For non-PPCD plasmas with $T_e < 1$ keV, the signal from thermal electrons above 5-6 keV is expected to be negligible. Simultaneous measurements were also made using a fast (sub-μs) energy-resolved single-chord detector based on a Si avalanche photodiode, referred to as the "fast x-ray" (FXR) detector[23], for comparison.

FIG. 6 presents data from a 500 kA QSH plasma: (a) shows the development of the dominant mode, while (b) and (c) show the corresponding FXR and ME-SXR measurements. A strongly non-thermal

population develops around 20 ms as the core-most resonant mode grows to dominate the spectrum, and this population is sustained for around 5 ms before terminating with a burst and then becoming mostly thermal again as the magnetic equilibrium evolves. Combined with simultaneous thermal measurements, these observations helped build an understanding of how confinement properties vary over the lifetime of a QSH plasma[9]. Note the logarithmic scale on the axis of the ME-SXR data. The close correspondence between between the FXR and ME-SXR photon flux provides confidence in the accuracy of the measurements and in the usefulness of the ME-SXR as a standalone runaway electron diagnostic.

The ME-SXR diagnostic was also used to study the runaway electrons present when the MST is operated like a tokamak. A clear correlation was observed between decreasing density and increasing photon flux. These observations are reported in L.F. Delgado-Aparicio's contribution to these proceedings[5].

VII. INTEGRATED DATA ANALYSIS

Section V provided a straightforward technique to extract T_e measurements with minimal *a-priori* assumptions. However, oftentimes additional information is available, such as concurrent measurements from other diagnostics, previous results, and knowledge of the underlying physics. This section presents a consistent way of incorporating all of this additional information into a single framework, called integrated data analysis (IDA)[17]. With this framework we will be able to simultaneously produce measurements of the electron temperature and impurity ion densities, demonstrating the versatility of the ME-SXR diagnostic.

The IDA methodology demonstrated here is based on Bayesian inference[13]. This is an approach to probability which views probability as the quantification of the degree of certainty based on the available information, rather than than the long-term frequency over many repetitions. The heart of Bayesian inference is Bayes' Rule[24],

$$p(\boldsymbol{\theta}|\boldsymbol{d},I) \propto p(\boldsymbol{d}|\boldsymbol{\theta},I)\, p(\boldsymbol{\theta}|I), \tag{8}$$

which states that the *posterior* $p(\boldsymbol{\theta}|\boldsymbol{d},I)$ of a system being best-described by the parameter vector $\boldsymbol{\theta}$ given some measured data $\boldsymbol{d}$ is proportional to the product of the *likelihood* $p(\boldsymbol{d}|\boldsymbol{\theta},I)$ of having measured that data given the parameter vector and the *prior* information $p(\boldsymbol{\theta}|I)$. The I in Bayes' rules is meant to represent the additional information that has been incorporated into the analysis, such as the choice of a particular model.

Bayes' Rule is intended to be applied iteratively whenever new information is made available. The approach to IDA employed here takes advantage of this feature to iteratively apply Bayes' Rule with simultaneous measurements from independent diagnostics, taking advantage of all available information to make the best possible estimate of the model parameters[17]. This approach allows the data analyst to exploit the ways in which different diagnostic measurements correlate the plasma properties, sometimes enabling estimates of properties (like Z_{eff} in the RFP) that cannot be readily measured by a single dedicated diagnostic[25]. This approach will also provide a natural and consistent framework for propagating measurement uncertainty, including when the underlying distributions are not Gaussian.

The aim of this section is to provide a full, detailed example of how to implement the ME-SXR diagnostic into an IDA framework. Two versions of the analysis will be performed. The first will incorporate just the ME-SXR and Thomson scattering diagnostics (termed "ME-SXR+TS"), while the second will also include measurements from a complimentary SXR tomography array[26] (termed "Full IDA"). The first analysis will allow us to demonstrate the ME-SXR diagnostic's sensitivity to mid-Z impurities (like Al), while the second will refine these results to provide the best estimates of the plasma profiles given all available data. A PPCD plasma was chosen to be the test case since PPCD plasmas have been thoroughly studied, meaning we can make use of well-informed priors. Section VII A begins by describing the PPCD plasma model. Section VII B then goes through the process of correctly selecting likelihood and prior distributions based on the best available information. Section VII C presents the results of the ME-SXR + TS analysis, demonstrating good sensitivity to Z_{eff}. Finally, Section VII D presents the results of full IDA analysis, and draws comparisons.

A. The PPCD plasma model

Previous experience on MST has found that the temperature and density profiles in high-current PPCD plasmas are well-described by the aforementioned "α-β"model. Additional features such as islands or hollow rings can be included as additional terms if needed. The temperature profile is modeled as

$$T_e(\rho) = T_{e,0}\left(1-\rho^{\alpha_T}\right)^{\beta_T}, \tag{9}$$

where ρ is the normalized MSTFit[16] radial flux surface label. The value of β_T is typically fixed, as it tends to be semi-redundant with the α_T parameter. An MSTFit reconstruction will be used to provide the mapping between ρ and standard Cartesian spatial coordinates (x,y), as well as a reconstructed $n_e(\rho)$ profile.

MST plasmas typically feature several impurity species in concentration high enough to measurably impact the SXR spectrum: N and O from air, C from graphite in the limiter, B from probes, and Al from the vacuum vessel wall. Ar can also be doped into MST, but is not otherwise present in significant concentrations. It has been established that during PPCD discharges these ions are subject to a classical transport effect known as temperature screening[27]. Essentially, the presence of an ion temperature gradient leads to an expulsion of impurity ions from the core of the plasma, resulting in a hollow profile shape which peaks at the outer mid-radius. These predictions have been experimentally confirmed with charge-exchange recombination spectroscopy measurements[28]. The PPCD plasma model accounts for this phenomenon by adding an additional "hollow bump" term to the standard "α-β" density profile, given by

$$n_Z(\rho) = n_{Z,0}\left(1-\rho^{\alpha}\right)^{\beta} + \delta n_Z \exp\left(-\frac{(\rho-\delta r/a)^2}{2(w_r/a)^2}\right), \tag{10}$$

where n_Z refers to the total impurity species density (including all ionization states), δn_Z refers to the increased accumulation at the hollow bump for the impurity species Z, $\delta r/a$ is the normalized location of the bump and w_r/a is the normalized width of the bump. α_Z, β_Z, δr, and w_r are assumed to be the same for all impurity species.

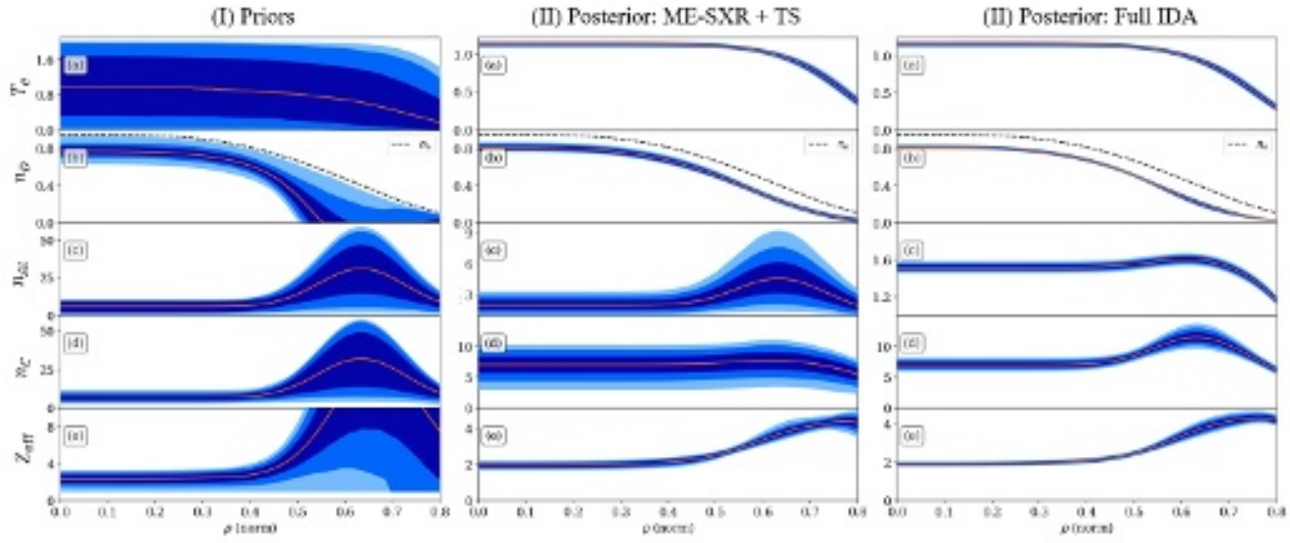

FIG. 7. Prior (I) and posterior (II, III) distributions over the (a) electron temperature, (b) deuterium density, and (c) aluminum density, (d) carbon density, and (e) ion-effective charge (Z_{eff}) profiles. The orange line represents the median profile and the shaded regions encompass the 1-, 2-, and 3-σ credibility regions.

Rather than treat all impurity ion densities as free parameters, only n_C is treated as a free parameter, while the remaining low-Z impurities are constrained based on empirically-established ratios[25]: $n_O/n_C = 0.9$, $n_N/n_C = 0.3$, and $n_B/n_C = 0.3$. As these species all tend to be fully-ionized and do not feature recombination steps or lines in the SXR spectrum, they essentially just serve to contribute to the overall Z_{eff}. This means that any analysis routine using this model would not be able to meaningfully distinguish between, for instance, an increase in n_C vs an increase in n_O. Al ions in the MST, however, are not fully ionized, so n_{Al} is left as a additional free parameter.

Finally, a fixed neutral density model was included based on previous measurements[29]. This profile is flat throughout the core but grows exponentially by two orders of magnitude near the edge. The presence of a finite neutral density has been found to significantly affect the ionization balance in MST plasmas[9].

As implemented, the model has six free parameters represented in the parameter vector,

$$\boldsymbol{\theta} = (T_{e,0}, \alpha_T, n_{Al,0}, n_{C,0}, \delta n_{Al}, \delta n_C). \tag{11}$$

The remaining parameters are held fixed at the default values. This set of parameters was settled upon as a compromise between model flexibility (including more parameters) and computational requirements (models with fewer parameters converge more quickly).

B. Likelihood and priors

A summary of all the parameters which describe the PPCD plamsa model, and their default values, is given in TABLE I. Most of the priors were taken to be uniform with bounds given by the [Min,Max] values listed in the table. This equates to an assertion that the probability of that parameter taking on any value within this range is equal, while any value outside of this range has a probability of zero. These

PPCD model parameters

Parameter	Units	Default	Min	Max
$T_{e,0}$	eV	1100	0	2000
α_T	N/A	7	2	14
β_T	N/A	7		Fixed
$n_{Al,0}$	10^{19} m^{-3}	2e-3	1e-4	1e-2
$n_{C,0}$	10^{19} m^{-3}	6.8e-3	$\mathcal{N}(2.8e-3, 1.4e-3)$	
α_Z	N/A	12		Fixed
β_Z	N/A	4		Fixed
δn_{Al}	10^{19} m^{-3}	2.5e-3	1e-4	1e-2
δn_C	10^{19} m^{-3}	1.8e-2	1e-4	5e-2
$\delta r/a$	N/A	0.635		Fixed
w_r/a	N/A	0.09		Fixed

TABLE I. List of PPCD model parameters, including units, default values, and [Min, Max] range for uniform priors. Parameters which are fixed in the model are noted.

bounds were mostly chosen by physical considerations ($T_{e,0}$ must be positive) or constrained by previous expectations ($T_{e,0} > 2$ keV is implausible for these bank settings). The one exception is the core carbon density, which was assigned a Gaussian prior based upon an ensemble of previous charge exchange recombination spectroscopy measurements[25]. It is assumed to have a mean of $\mu_C = 2.8$e-3 and a standard deviation of $\sigma_C = 1.4$e-3, measured in the units shown in Table I. The range of profiles permitted by this selection of priors is illustrated in FIG. 7 (I).

A likelihood function was chosen for each diagnostic (ME-SXR, Thomson, and SXR tomography). Each likelihood model, which quantifies the probability that one might have measured the data d given some known parameters $\boldsymbol{\theta}$, was chosen by combining the relevant diagnostic forward model[11,30] with a statistical model of the measurement noise. For each case the measurement noise was as-

sumed to be Gaussian, giving a general form of

$$\ln p(\boldsymbol{d}|\boldsymbol{\theta},I) = -\frac{1}{2}\sum_i^N \left(\frac{d_i - f(p_i,\boldsymbol{\theta})}{\sigma_i}\right)^2, \tag{12}$$

where $f(p_i,\boldsymbol{\theta})$ is the diagnostic forward model for the i$^{\text{th}}$ pixel given the chord radius p_i, and $\sigma_i^2 = \sigma_{d,i}^2 + \sigma_{m,i}^2$ where $\sigma_{d,i}$ is the measurement noise and $\sigma_{d,i}$ is the systematic uncertainty in the model. The uncertainty σ_m for the ME-SXR forward model was found to be around 15%, due mostly to uncertainty in the Mylar filter thickness[9]. For the SXR tomography model, the uncertainty σ_m was taken to be 2%[31].

Although the noise model for the ME-SXR diagnostic is more properly described by a Poisson distribution, given the relatively high count rates during PPCD the Gaussian approximation $\sigma_{d,i} \approx \sqrt{N}$ was considered to be adequate.

The likelihoods were combined via an iterative application of Bayes' Rule, yielding the posterior distribution. For the ME-SXR + TS analysis this is given by

$$p_1(\boldsymbol{\theta}|\boldsymbol{D}_1,I) \propto p_{\text{MESXR}}(\boldsymbol{d}_{\text{MESXR}}|\boldsymbol{\theta},I)\, p_{\text{TS}}(\boldsymbol{d}_{\text{TS}}|\boldsymbol{\theta},I)\, p(\boldsymbol{\theta}|I), \tag{13}$$

where $\boldsymbol{D}_1 = (\boldsymbol{d}_{\text{MESXR}}, \boldsymbol{d}_{\text{TS}})$. For the full IDA framework (ME-SXR + TS + SXT), the likelihood is given by

$$\begin{aligned} p_2(\boldsymbol{\theta}|\boldsymbol{D}_2,I) \propto\ & p_{\text{MESXR}}(\boldsymbol{d}_{\text{MESXR}}|\boldsymbol{\theta},I)\, p_{\text{SXT}}(\boldsymbol{d}_{\text{SXT}}|\boldsymbol{\theta},I) \\ & \times p_{\text{N2}}(\boldsymbol{d}_{\text{N2}}|\boldsymbol{\theta},I)\, p_{\text{TS}}(\boldsymbol{d}_{\text{TS}}|\boldsymbol{\theta},I)\, p(\boldsymbol{\theta}|I), \end{aligned} \tag{14}$$

where $\boldsymbol{D}_2 = (\boldsymbol{d}_{\text{MESXR}}, \boldsymbol{d}_{\text{SXT}}, \boldsymbol{d}_{\text{N2}}, \boldsymbol{d}_{\text{TS}})$. The posterior distribution describes how well a given set of parameters $\boldsymbol{\theta}$ describes the data $\boldsymbol{D}$, so the process of model-fitting is replaced with drawing many samples from this distribution and analyzing their statistical properties.

C. Results: ME-SXR + TS

This analysis was performed for a single time point (averaged over 1 millisecond) near the end of the enhanced confinement period of a 300 kA PPCD plasma. The posterior distribution $p_1(\boldsymbol{\theta}|\boldsymbol{D}_1,I)$ was sampled using the `emcee` MCMC sampling software[32] until good convergence was achieved.

N samples were drawn from the posterior distribution, $\{\hat{\boldsymbol{\theta}}_1, \hat{\boldsymbol{\theta}}_2, \ldots, \hat{\boldsymbol{\theta}}_N\}$, which were used to produce an ensemble of N plasma profiles, i.e. $\{T_e(\rho|\hat{\boldsymbol{\theta}}_1)\}, \{T_e(\rho|\hat{\boldsymbol{\theta}}_2)\}, \ldots, \{T_e(\rho|\hat{\boldsymbol{\theta}}_N)\}$ for the temperature profile, each of which were calculated over a grid of 100 ρ points. This ensemble was used to estimate the median profile, $\langle T_e(\rho)\rangle$, and the 65%, 95%, and 99.7% credibility regions (the Bayesian equivalent to 1-, 2-, and 3-σ confidence intervals[33]) at each point. These profile samples are shown in FIG. 7 (II.a), (II.c), and (II.d). The ensemble of profiles can also be used to compute the profiles for derived quantities, like n_D and Z_{eff}, shown in (II.b) and (II.d) respectively. These profiles are the primary result of this analysis.

The integration of ME-SXR and Thomson scattering data allows for a highly accurate estimate of the core electron temperature, $T_e = 1125 \pm 12$ eV. The ion densities have also been well-constrained compared to the priors, with core values of $n_{Al} = 1.99 \pm 0.44 \times 10^{16}$ m^{-3} and $n_C = 7.01 \pm 1.3 \times 10^{16}$ m^{-3}. However, because the n_C profile is actually a stand-in for all of the low-Z impurities (C, B, O, and N), its individual value is not necessarily physically meaningful. Instead, the important result is the Z_{eff} profile, which is well-constrained to $Z_{\text{eff}} = 1.97 \pm 0.08$ in the core. This is consistent with previous estimates using other diagnostics[25].

This analysis does not, however, do a good job constraining the ion density profiles outside of the core. This is because the ME-SXR model, with the 100 μm filter, has difficulty discerning between n_{Al} and n_C in the lower-signal regions. This results in a strong correlation between n_{Al}, n_C, and δn_{Al} in the posterior distribution. The overall estimate for Z_{eff}, however, is relatively well-constrained. The high uncertainty in the individual measurements presents a significant opportunity for additional diagnostics to improve these results. Even so, the obtained profiles represent a significant improvement over the priors $p(\boldsymbol{\theta}|I)$.

Overall, these results serve as a demonstration that the ME-SXR diagnostic, when combined with Thomson scattering, can be used to reconstruct T_e, n_{Al}, and Z_{eff} profiles which are well-constrained in the core. These results are both more accurate and more informative than the direct T_e inversion methods previously discussed, although they require more information and assumptions about the underlying plasma equilibrium. Uncertainty in the ion densities is still large in the edge, though, providing an opportunity for additional diagnostics to further constrain the results. This is accomplished in the next section by the inclusion of the SXR tomography diagnostic, which, equipped with 45/172 μm Be filter pairs, is expected to provide increased sensitivity to the Al line emissions.

D. Results: Full IDA

The analysis was repeated with the full likelihood function $p_2(\boldsymbol{\theta}|\boldsymbol{D}_2,I)$, which incorporates the SXR tomography data and forward model. The posterior was again sampled, with the resulting profiles and credible intervals shown in FIG. 7 (III). In comparison to the ME-SXR + TS analysis, the addition of new measurements has done little to affect the T_e profile. However, the ion density profiles have been significantly refined with n_C now clearly demonstrating a hollow profile while n_{Al} nearly flat. The core values have also been further refined, especially n_{Al}. However, the change to the resulting Z_{eff} profile is modest. The new profiles are all within the uncertainty bands of the previous analysis (FIG. 7 (II)).

The best way to assess the quality of a fit is to compare the output of the models with the original measured data. This too is accomplished through sampling. For each diagnostic, the forward model is calculated for each profile in the ensemble. This produces an ensemble of synthetic measurements for each channel, which are then analyzed statistically. Because these ensembles tend to be very nearly Gaussian, they are well-characterized by the mean and standard deviation. FIG. 8 shows this data/model comparison for the ME-SXR, Thomson scattering, and SXR tomography diagnostics. The agreement, though not perfect, is generally good. Some level of disagreement is to be expected when simultaneously fitting multiple models, each with their own sources of uncorrelated systematic uncertainty. This is in-fact a feature of IDA, and is the reason we included the σ_m terms in the likelihood functions. The fact that all three diagnostics are in good agreement with the synthetic measurements, and that the

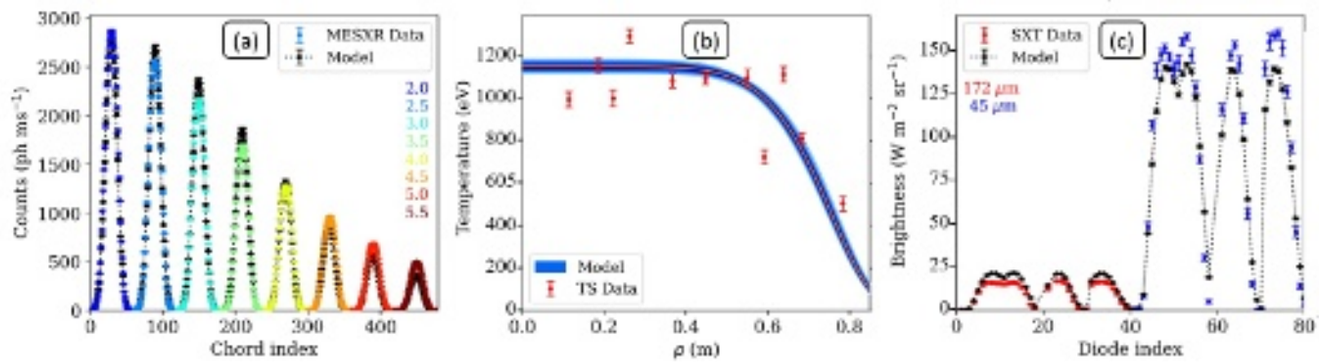

FIG. 8. Comparison between diagnostic data and model output for the Full IDA results for the (a) ME-SXR, (b) Thomson scattering, and (c) SXR tomography diagnostics.

resulting profiles are in good agreement with prior results, lends a significant amount to confidence in the ME-SXR forward model.

VIII. CONCLUSION

The versatility of the ME-SXR diagnostic for characterizing multiple properties of a magnetically-confined fusion plasma has been demonstrated. The ME-SXR diagnostic was used to observe plasma temporal evolution. Photon counts were seen to evolve appropriately as the plasma heats up, and decrease as the plasma cools. A method for identifying the energy of an emission line was presented, and tested using Ar-doped plasmas. A technique for determining the electron temperature profile by directly inverting the emissivity was shown to agree with Thomson scattering measurements up to an ~ 180 eV offset, which may be due to the presence of background hard x-rays from the runaway population known to develop during PPCD. Runaway electrons were observed to form during helical plasmas in the MST, and their population was correlated to the evolution of the magnetic equilibrium. The ME-SXR diagnostic was also incorporated into an integrated data analysis (IDA) framework based on Bayesian inference. Using this methodology, it was shown to be possible to simultaneously extract T_e and n_Z profiles from ME-SXR and Thomson scattering data. The resulting profiles can be further refined by including the SXR tomography diagnostic in the analysis. The ability to simultaneously fit multiple diagnostics to their respective data using physically-reasonable profiles provides a high level of confidence for the ME-SXR forward model.

ACKNOWLEDGEMENTS

This work is supported by the U.S. Department of Energy Office of Science, Office of Fusion Energy Sciences program under Awards No. DE-SC0018266 and DE-SC0015474.

DATA AVAILABILITY

The data that support the findings of this study are available from the corresponding author upon reasonable request.

[1]N. Pablant, *et al.* Review of Scientific Instruments **83** (2012), 10.1063/1.4732177.
[2]R. N. Dexter, *et al.*, Fusion Technology **19**, 131 (1991).
[3]J. Sarff, *et al.*, Physical Review Letters **72** (1994).
[4]B. E. Chapman, *et al.*, Plasma Physics and Controlled Fusion **52** (2010), 10.1088/0741-3335/52/12/124048.
[5]L. Delgado-Aparicio, *et al.*, Review of Scientific Instruments **91** TBD (2021).
[6]O. Chellai, *et al.*, Review of Scientific Instruments **91** TBD (2021).
[7]T. Barbui, *et al.*, Review of Scientific Instruments **91** TBD (2021).
[8]P. Kraft, *et al.*, , IEEE Transactions on Nuclear Science **56**, 758 (2009).
[9]P. D. VanMeter, *Observations of helical plasma dynamics using complementary x-ray diagnostics in the MST*, Ph.D. thesis, University of WIsconsin-Madison (2020).
[10]P. VanMeter, *et al.*, Review of Scientific Instruments **89** (2018), 10.1063/1.5037347.
[11]P. VanMeter, *et al.*, Journal of Instrumentation **14** (2019), 10.1088/1748-0221/14/09/C09009.
[12]A. Kramida, *et al.*, "NIST Atomic Spectra Database (ver. 5.6.1)," (2019).
[13]U. Von Toussaint, Reviews of Modern Physics **83**, 943 (2011).
[14]R. E. Bell, Review of Scientific Instruments **66**, 558 (1995).
[15]L. Delgado-Aparicio, *et al.*, Review of Scientific Instruments **89** (2018), 10.1063/1.5038798.
[16]J. K. Anderson, *et al.*, Nuclear Fusion **44**, 162 (2004).
[17]L. M. Reusch, *et al.*, Review of Scientific Instruments **89** (2018), 10.1063/1.5039349.
[18]D. Li, *et al.*, Review of Scientific Instruments **84**, 0 (2013).
[19]R. O'Connell, *et al.*, Physical Review Letters **91**, 8 (2003).
[20]D. F. Escande, *et al.*, Physical Review Letters **85**, 1662 (2000).
[21]P. Franz, *et al.*, Nuclear Fusion **53**, 053011 (2013).
[22]D. J. Clayton, *et al.*, Physics of Plasmas **17** (2010), 10.1063/1.3292658.
[23]A. M. Dubois, *et al.*, Review of Scientific Instruments **86**, 1 (2015).
[24]A. Gelman, *et al.*, *Bayesian Data Analysis*, 3rd ed. (CRC Press, Boca Raton, FL, 2014) p. 661.
[25]M. Galante, *et al.*, Nuclear Fusion **55**, 123016 (2015).
[26]P. Franz, *et al.*, Review of Scientific Instruments **75** (2004), 10.1063/1.1794845.
[27]S. T. Kumar, *et al.*, Physical Review Letters **108**, 3 (2012).
[28]S. T. Kumar, *et al.*, Plasma Physics and Controlled Fusion **54** (2012), 10.1088/0741-3335/54/1/012002.
[29]Z. A. Xing, *Ion Thermal Transport and Heating in Reduced Tearing RFP*, Ph.D. thesis, University of Wisconsin-Madison (2019).
[30]L. M. Reusch, *et al.*, Fusion Science and Technology **74**, 167 (2018).
[31]J. Johnson, "Implementing Bayesian Statistics and a Full Systematic Uncertainty Propagation with the Soft X-Ray Tomography Diagnostic on the Madison Symmetric Torus (undergraduate thesis)," Tech. Rep. (University of Wisconsin-Madison, Madison, 2013).
[32]D. Foreman-Mackey, *et al.*, Publications of the Royal Astronomical Society of the Pacific **125**, 306 (2013).
[33]M. D. Nornberg, *et al.*, Fusion Science and Technology **74**, 144 (2018).